

Aluminum oxidation in Ar-O₂ dielectric-barrier discharges and -post-discharges – the roles of atomic oxygen and 9.8-eV photons

M. Betz¹, L. Bröcker¹, A. Jung¹, V. Raev¹, R. Bandorf², H. Gerdes², and C.-P. Klages¹

¹ Institute for Surface Technology (IOT), Technische Universität Braunschweig, Braunschweig, Germany

² Fraunhofer Institute for Surface Engineering and Thin Films (IST), Braunschweig, Germany

Abstract: Room-temperature oxidation of aluminum is strongly enhanced by the exposure to atmospheric-pressure dielectric-barrier discharges (DBDs) and post-discharges in Ar-O₂ mixtures. The contribution is focussed on the roles of oxygen atoms and of photons with energies beyond the oxide band gap, produced in the DBD. To enable an independent variation of O-atom densities and surface-flux of photons, a special F-shaped double-DBD reactor was designed. Results are discussed within Cabrera-Mott theory of metal oxidation.

Keywords: DBD, post-discharge, oxygen, VUV, metal oxidation, aluminum, Al₂O₃

1. Introduction

Thermal oxidation of aluminum at low temperature is self-limiting in the sense that the oxide grows relatively fast to a certain thickness X (“limiting thickness”) beyond which the oxidation rate is much slower. After exposure to the ambient at room temperature, thicknesses of 3.1 and 3.4 nm, respectively, were measured on (100) and (111) surfaces of Al single crystals, virtually constant over one year (3×10^7 s) [1]. The theory developed by Cabrera and Mott (CM) [2] explains low-temperature growth of metal oxides by the establishment of a negative electrical potential, the later so-called Mott potential, V_M , by negative charging of oxygen species adsorbed on the oxide surface, due to transfer of electrons from the metal to adsorbed oxygen. The resulting electric field lowers the potential barrier which mobile Al³⁺ ions have to overcome to be injected from the metal into the oxide and to drift to the oxide/gas interface where they recombine with counterions. The theory was significantly advanced by Fromhold and Cook, taking into account the coupling of electric current carried by electrons, J_e , with the ion current, J_i , imposing the condition that the sum of currents must be zero, see refs. [3, 4] and citations therein.

To achieve low-temperature oxide growth beyond thicknesses in the lower nm range and to enable a control of oxide properties, several plasma oxidation studies have been conducted. A contribution by Rider et al. [5] deserves special attention because low-pressure (10.5 Pa O₂ or H₂O) radio-frequency (125 kHz) plasma oxidation of Al was interpreted in terms of CM theory. Parameters X_1 and u of CM’s fundamental differential equation (1) for $X(t)$ were calculated. X_1 is proportional to $|V_M|/T$.

$$dX/dt = 2 \times u \times \sinh(X_1/X) \quad (1)$$

The present contribution is focussed on the roles of atomic oxygen and vacuum ultraviolet (VUV) radiation on plasma-assisted oxide growth at atmospheric pressure. O atoms and 9.8-eV photons are generated efficiently in Ar-O₂ DBDs with small O₂ fractions (typically less than 0.1 %) by dissociation and excitation/radiation processes.

Oxidation of sputtered Al films on Si substrates, exposed directly to the DBD and to the post-discharge (PoD), respectively (Fig. 1), were studied, using infrared absorption-reflexion spectroscopy (IRRAS) as a routine method for thickness measurement, calibrated by XPS. Studying

the effects of substrate irradiation in a special reactor (see Fig. 2) was motivated by the observation of substantial oxide growth in the pre-discharge (PrD) region, inaccessible for species generated in the DBD except for photons.

2. Experimental

Figs. 1. and 2. show schematics of the flow-through DBD reactor and of the F-shaped reactor with two DBDs, A and B, respectively, used for the present study.

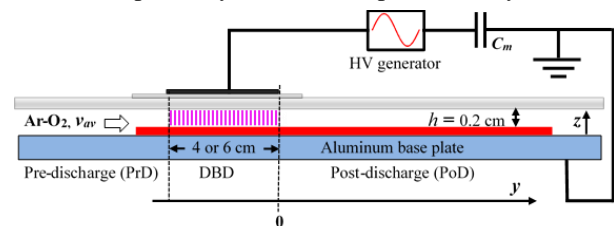


Fig. 1. DBD reactor I: grounded Al base plate and glass dielectric as top boundary of the flow channel. Red stripe: gapless row of up to 15 Al/Si samples. Process parameters usually were: 16 kHz, 3.6 kV amp., 1.2 Wcm⁻³ power density, average gas velocity v_{av} was 150 cms⁻¹.

Studied samples were Al films, magnetron-DC-sputtered on 1×2 cm² Si substrates in an in-line coating system with load lock and three process chambers, equipped with a planar Al target (purity 99.999 %). Base pressure was below 1×10^{-4} Pa, operating pressure 1 Pa. Process gas was Ar (purity 5.0), with a gas flow of 200 cm³/min STP.

For oxidation experiments, process gases Ar and O₂ were of purity 6.0. Oxidation experiments were performed by first measuring samples by IRRAS to determine $X(0)$. Then the samples were charged into the reactor, oxidized for m min (mostly $m = 5$ or 10 min), measured again, oxidized for another m min, measured, oxidized $2 \times m$ min and so on, up to the maximum oxidation time, t . As a routine method to determine X , FTIR measurements were performed in the infrared-reflexion absorption (IRRAS) mode at an angle of 80°, using a Nicolet iS50 spectrometer (Thermo Fisher Scientific GmbH, Dreieich, Germany). In oxidation experiments with Reactor I X was obtained from the wavenumber-integrated absorbance of the LO mode of Al₂O₃, peaking near 950 cm⁻¹ [6]. Integration limits were 1050 and 750 cm⁻¹, respectively. The method was

calibrated using 15 XPS measurements of X [7] on samples with $3.5 < X/\text{nm} < 7.0$.

The average oxide starting thickness on the samples, prepared typically 3 months before they were used in this study, had grown to between 3.1 and 3.6 nm, in agreement with Evertsson et al. [1], close to the “limiting thickness” under ambient conditions, in the sense of the original CM theory. Nevertheless the oxide thickness achieved within most of the here-reported experiments at the lowest oxidation duration of 5 min was generally sufficient to obtain a thickness which was virtually the same as if oxidation had started with $X(0) = 0$ nm, due to the characteristic time-dependence of $X(t)$.

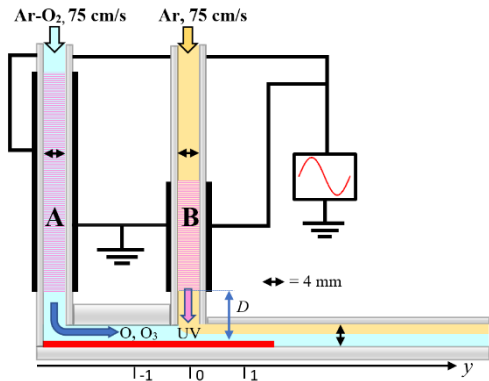


Fig. 2. F-shaped double-DBD reactor II. Red: samples; plasma A and B driven by sinusoidal voltage at 40 kHz, 5 kV amp. and with 1.1 W cm^{-3} power density.

For experiments with reactor II, $X(t)$ data were evaluated from absorbance differences $\Delta A \equiv A(\text{peak}) - A(1050 \text{ cm}^{-1})$, to avoid errors inherent in the integration method, caused by an unidentified chemisorbed oxygen species absorbing between 600 to 800 cm^{-1} [8]. Oxidized samples were also characterized by ex-situ-measurements of Volta-potential differences (VPD) relative to a gold surface, using an ambient single-point Kelvin probe from *Anfatec Instruments AG* (Oelsnitz, Germany). The measured VPD is the difference of work functions: $VPD = \phi_{Au} - \phi_{\text{Sample}}$ [9]. The measurements were done before and immediately after oxidation steps and, for selected samples, over time, up to several weeks.

For an analysis of data in terms of the original CM theory, equation $X^{-1} = A - B \times \ln(t)$ was used as an empirical equation to determine A and B from experimental $X(t)$ data by linear regression. Then an empirical analytical expression for $dX(t)/dt$ was calculated, equated to the right-hand side of equation (1), and the resulting equation was fitted to the original $X(t)$ data, using the nonlinear implicit fit facility of *OriginPro*. Resulting X_I and u were applied to generate $X(t)$ graphs numerically from equation (1). In the following, such graphs are shown as solid curves. Frequently, this procedure failed beyond certain values of X , typically between 5.5 and 6 nm, most probably due to vanishing electron conduction, which is required to compensate for the ion current [3]. In such cases the inverse logarithmic plot has significant positive outliers which were not included in the CM evaluation, see the

example in Figures 5, using data obtained in reactor II with 20 ppm O_2 , without VUV, at position $y = -1$ cm: Here, the oxide growth finds a virtual end at 5.7 nm.

3. Results

Reactor I: Fig. 3 shows oxide growth $X(t)$ in the pre-discharge region, 1.5 or 0.5 cm from the leading plasma edge (“PrD1.5” etc.), at one position within the downstream region of the DBD (“DBD”), and at several positions in the post-discharge, 1, 3, and 5 cm, respectively, behind the trailing plasma edge (“PoD1” etc.). Pairs of numbers like “1.19E-9/50.8” are parameters $u/\text{nm} \times \text{s}^{-1}$ and X_I/nm obtained as outlined above. An arrow with a cross marks an outlier excluded from the evaluation. Arrows with an oval mark overlapping data points.

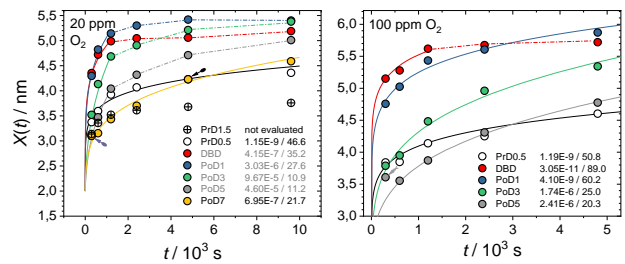


Fig. 3. $X(t)$ at different positions in reactor I, at 1.2 W cm^{-3} power density, 150 cm/s gas velocity, input O_2 fractions 20 ppm (left) and 100 ppm (right), respectively, see text for explanations. (Data with 20 ppm at O_2 PrD1.5 could not be evaluated by the procedure described above. Note that X at PoD1 and PoD3 is larger than in the DBD.)

Aside from substantial oxidation in the PoD, even at $y = 7$ cm in case of $x_{\text{O}_2} = 20$ ppm, significant oxide growth takes place at least up to 1.5 cm upstream from the DBD: Thickness increments ΔX at PrD1.5 are still about 50 % of ΔX at PrD0.5. Oxidation ahead from the DBD can neither be due (i) to counter-stream diffusion of atomic oxygen from the DBD, as to be seen by CFD simulation, nor (ii) to volume generation of O atoms by photodissociation in the inflowing gas, due to the too small cross sections [10].

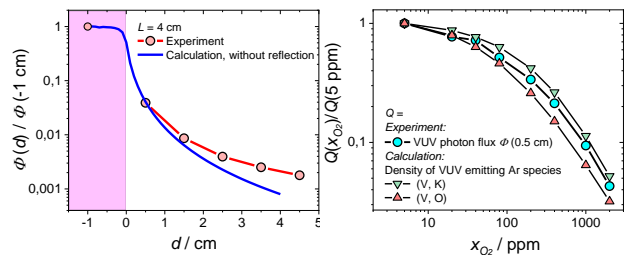


Fig. 4. Surface flux of VUV photons, Φ , as (i) a function of distance d from the DBD edge ($d < 0$ is a location within the DBD) (lhs) and (ii), normalized, the input fraction of oxygen, x_{O_2} (rhs), respectively. L is the discharge length.

Therefore, we conclude that surface irradiation by vacuum ultraviolet (VUV) photons from the DBD oxidation must be responsible for the effects, in spite of the

rapid decay of photon flux to the surface, $\Phi(d)$, with growing distance d from the DBD edge: Fig. 4, lhs, shows the decay of $\Phi(d)$. On the right, the quenching effect of O_2 is shown. The experimental data were obtained by optical emission measurements in the visible range on scintillator dots from pressed sodium salicylate powder [11].

Reactor II: To enable an independent variation of the O atom density, n_o , and the flux of VUV photons to the surface, Φ , experiments were run in the F-shaped double-DBD reactor shown in Figure 2. Here, $n_o(y)$ decays with growing y due to recombination. $\Phi(0)$ can be controlled by the distance, D , of the DBD edge in the 2nd vertical channel from the substrate surface, see Fig. 1.

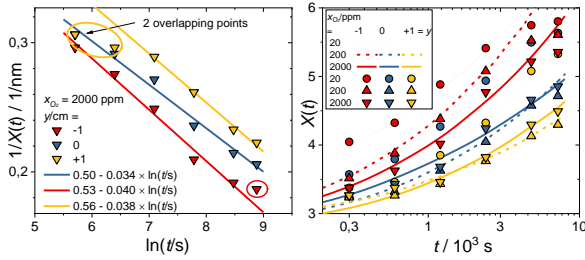


Fig. 5. O-atom-induced oxidation at $y = -1, 0$, and 1 cm, respectively, in Ar- O_2 . Only DBD A on. Lhs: Inverse log plot, excluded data points encircled. On the rhs, data are fitted using equation (1). For fit parameters and excluded samples, see Table 1. Note the logarithmic t scale.

Fig. 5 shows results of experiments in which only DBD A was on, i. e., samples were not VUV-irradiated. On the lhs an inverse logarithmic plot is shown for $x_{O_2} = 2000$ ppm: For the CM fit on the rhs, some data had to be excluded (i) at small t due to too large $X(0)$ and (ii) at large t due to the approach to a limiting thickness which we abbreviate as LT_2 in order to stress the difference from MC's limiting thickness, LT_{CM} , a mathematical construct depending on the definition of an observation time scale. Numbers of excluded samples are 1 for the 5-min oxidation, n for the last oxidation step, etc., see Table 1 with fit parameters. The last column shows densities of O atoms and O_3 , calculated with a recently-published plug-flow model [12]. VPD data for $x_{O_2} = 20$ ppm are shown below in Fig. 6, lhs, together with a linear regression of data at $y = -1$ cm.

Table 1. Fit parameters for Fig. 5, rhs.

x_{O_2} ppm	y cm	$u \times 10^6$ nm/s	X_l nm	# excl.	n_o	n_{O_3}
					10^{14} cm^{-3}	
20	-1	5.52	22.8	n-1, n	3.0	0.33
	0	9.26	17.8	n	2.4	0.41
	1	10.2	15.2	1	2.2	0.45
200	-1	23.2	15.0	n-1, n	3.0	13
	0	4.02	17.1	1, n	2.1	14
	1	0.27	24.6	1	1.9	14
2000	-1	9.43	16.7	n	0.13	190
	0	1.41	21.5	-	0.06	190
	1	2.02	11.8	1, 2	0.04	190

If only the VUV-generating DBD is operative (DBDs A off, B on), surprisingly similar oxide thicknesses $X(t)$ are obtained at $y = 0$ for oxygen molar fractions of 20, 200, and 2000 ppm, respectively, see Figure 6, rhs. (Virtually the same results were obtained with nominally pure Ar 6.0, i. e., with oxygen impurities of about 1 ppm.) In the same figure VPD values are shown, obtained about a few min after the oxidation step. As in the case of O-atom-driven oxidation (Fig. 6. lhs), VPD generally decreases with growing $X(t)$.

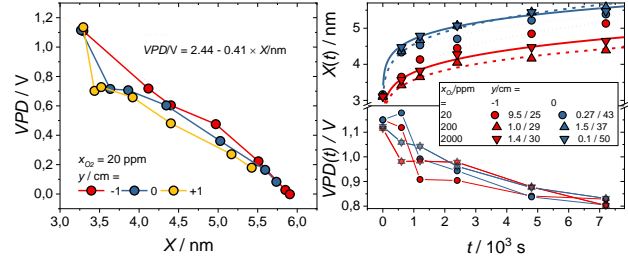


Fig. 6. Lhs: VPD of freshly treated films directly after O-atom-driven oxidation (DBD A on, B off, $x_{O_2} = 20$ ppm), vs. X . Rhs: VUV-induced oxidation of Al at $y = 0$ and -1 (DBD A off, B on), dependence on x_{O_2} . Pairs of numbers in the legend are $u/10^{-7} \text{ nm} \times \text{s}^{-1} / X_l/\text{nm}$. CM plots include all data. Lower part: $VPD(t)$ of the freshly oxidized samples.

With both DBDs, A and B on, samples are exposed simultaneously to atomic oxygen and/or ozone and VUV radiation. Selected results are shown in Fig. 7.

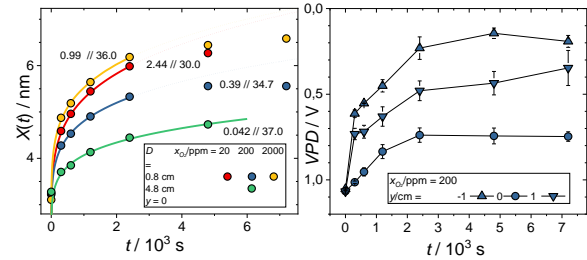


Fig. 7. Lhs: Oxidation of aluminum at $y = 0$, with DBDs A and B on, dependence on x_{O_2} and D . Figures at curves are $u/10^{-6} \text{ nm} \times \text{s}^{-1}, X_l/\text{nm}$. Rhs: $VPD(t)$ for $x_{O_2} = 200$ ppm at $y/\text{cm} = -1, 0, 1$. Note the inverted VPD scale.

Oxide thicknesses beyond 6.5 nm, achieved with 2000 ppm O_2 , where the afterglow is rich in O_3 , are the largest obtained in this study, but at least up to 4800 s results are similar for 20 and 2000 ppm O_2 while $X(200 \text{ ppm})$ stays significantly smaller. Reducing the photon flux by about an order of magnitude by increasing D (Fig. 2) from 0.8 to 4.8 cm lowers u by a factor of about 10. X_l values are between 30 and 37 nm; for the reliability of independent determination of u and X_l , consider the similarity of curves for $D = 0.8$ cm, 20 and 2000 ppm, respectively. In all experiments the decrease in VPD , i. e., increase of the work function ϕ_{Al/Al_2O_3} , parallels the increase of $X(t)$. With VUV irradiation, the change in VPD upon

oxidation is substantially smaller at $y=0$ than at less irradiated neighboring positions.

4. Discussion

Thermal oxidation of aluminum or Al alloys requires substantial temperatures, typically beyond 350 °C, in order to achieve an oxide thickness above about 5 nm [13]. While it is known since decades that plasma oxidation can strongly enhance low-temperature oxidation rate and oxide thicknesses, a detailed study of responsible factors was missing as yet. Even in the absence of strong VUV irradiation, thicknesses up to 5.8 nm can be achieved in DBD post-discharges with $n_O \approx 3.0 \times 10^{14} \text{ cm}^{-3}$. The $X(t)$ relation follows equation (1) from basic CM theory up to around 5.5 nm, with X_l in the range of 12 to 25 nm. In plasmas emitting energetic photons with energies beyond about 7 eV, several photophysical processes operative in the Al/Al₂O₃ system such as internal and external photoemission [14], and photoconduction [15] which may assist or impede oxidation. Photo-enhancement of aluminum oxidation was already reported by Cabrera in 1949 but the effects were relatively faint, $X(5 \text{ days})$ was 4 nm under irradiation with $1.6 \times 10^{15} \text{ cm}^{-2} \text{ s}^{-1}$ 4-eV photons [16]. The author predicted enhanced photo-oxidation with increased photon energy but, to our knowledge, the effect of super-bandgap radiation was not studied so far. In the experiments with reactor II, Φ was generally, at $D = 0.8 \text{ cm}$, about $3 \times 10^{15} \text{ cm}^{-2} \text{ s}^{-1}$ 9.8-eV photons. As these photons are hardly dissociating O₂ [10], a photophysical process within the Al/Al₂O₃ system is responsible for the observed enhancement, being virtually independent of x_{O_2} down to the low ppm range. For t up to 7800 s, $X(t)$ data at $y = -1$ and 0 cm could be fitted empirically by equation (1) with X_l in the range of 25 to 50 nm; at $y = 0$, thicknesses up to 5.5 nm were achieved. The combined action of active species generated in DBD A and VUV photons from DBD B enables oxide thicknesses beyond 6.5 nm to be reached within 2 h. Empirically, growth follows equation (1), with $30 \leq X_l/\text{nm} \leq 37$, up to a certain thickness beyond which the oxidation soon comes to a virtual halt when the limiting thickness, LT_2 , is approached.

$VPDs$ measured on freshly oxidized samples generally decrease with growing $X(t)$, strongest effects can be seen in the dark, see Fig. 6, lhs, where $VPD(20 \text{ ppm}, -1 \text{ cm})$ shows a nearly perfect correlation with corresponding X . An obvious explanation is the establishment of an electrical double layer, with a thin negatively charged zone at the oxide/air interface and a compensating positive layer at the metal/oxide boundary, with X -independent areal charge density, σ . A similar model has been applied to anodic oxide [17], the slopes $|dVPD/dX|$, however, were about an order of magnitude smaller than in the present study where we obtain, with $\epsilon_{Al_2O_3} = 9$ [17], interface and surface densities of 2.04×10^{13} elementary charges per cm^2 .

5. Conclusions

Low-temperature atmospheric-pressure oxidation of aluminum by DBDs and post-discharges in Ar-O₂ mixtures with $\leq 2000 \text{ ppm O}_2$ can be explained by the presence of O

atoms in combination with super-bandgap irradiation: Oxide thicknesses of 5.5 nm and beyond can be achieved by both, (i) exposure to the PoD of a DBD in Ar-O₂, even in the absence of strong VUV irradiation, and (ii) irradiation with 9.8-eV-photons in the presence of molecular O₂. Irradiating in the presence of O atoms results in the largest oxide thicknesses, up to 6.5 nm. Oxidation generally follows the basic CM equation for $X(t)$, up to a limiting thickness LT_2 , probably due to the decreasing electron transport.

The decreasing Volta potential difference VPD with increasing oxide thickness can be explained by an electric double layer with 2×10^{13} charges per cm^2 , negative at the surface, positive at the interface with the metal.

Acknowledgements

The authors acknowledge funding by the Deutsche Forschungsgemeinschaft, DFG (German Research Foundation) – project number 442139348.

6. References

- [1] J. Evertsson, F. Bertram, F. Zhang, L. Rullik, L. R. Merte, M. Shipilin, M. Soldemo, S. Ahmadi, N. Vinogradov, F. Carlà, J. Weissenrieder, M. Göthelid, J. Pan, A. Mikkelsen, J.-O. Nilsson, E. Lundgren, *Appl. Surf. Sci.* **349**, 826 (2015).
- [2] N. Cabrera, N. F. Mott, *Rep. Prog. Phys.* **12**, 163 (1949).
- [3] L. P. H. Jeurgens, A. Lyapin, E. J. Mittemeijer, *Acta Mater.* **53**, 4871 (2005).
- [4] F. Reichel, L. P. H. Jeurgens, E. J. Mittemeijer, *Acta Mater.* **56**, 2897 (2008).
- [5] A. N. Rider, R. N. Lamb, M. H. Koch, *Surf. Interface Anal.* **31**, 302 (2001).
- [6] E. Wäckelgård, *J. Phys.: Condens. Matter* **8**, 4289 (1996).
- [7] M. R. Alexander, G. E. Thompson, X. Zhou, N. Beamson, N. Fairley, *Surf. Interface Anal.* **34**, 485 (2002).
- [8] M. Che, A. J. Tench, *Adv. Catalys.* **32**, 1 (1983).
- [9] M. Henzler, W. Göpel, *Oberflächenphysik des Festkörpers*, B. G. Teubner, Stuttgart (1994).
- [10] A. N. Heays, A. D. Bosman, E. F. van Dishoeck, *Astronomy & Astrophysics* **602**, A105 (2017) A105. <https://www.uv-vis-spectral-atlas-mainz.org/>
- [11] B. Moine, G. Bizarri, B. Varrel, J.-Y. Rivoire, *Opt. Mat.* **29**, 1148 (2007).
- [12] C.-P. Klages, L. Bröcker, M. L. Betz, V. Raev, *Plasma Chem. Plasma Process.* **43**, 285 (2023).
- [13] J. Grimblot, J. M. Eldridge, *J. Electrochem. Soc.* **129**, 2369 (1982).
- [14] W. Pong, *J. Appl. Phys.* **40**, 1733 (1969).
- [15] J. L. Lauer, J. L. Shohet, C. Cismaru, R. W. Hansen, M. Y. Foo, T. J. Henn, *J. Appl. Phys.* **91**, 1242, (2002).
- [16] N. Cabrera, *Phil. Mag.* **40**, 175 (1949).
- [17] K. A. Yasakau, A. N. Salak, M. L. Zheludkevich, M. G. S. Ferreira, *J. Phys. Chem. C* **114**, 8474 (2010).